High-directional Vortex Beam Emitter Based on Archimedean Spiral Adiabatic Waveguides

SHIMAO LI,[1] WEN YU,[1] LAURA MERIGGI,[2] QINGSHENG XIAO,[1] ZHICHAO NONG,[1] XINLUN CAI,[1,*] MARC SOREL,[2] AND SIYUAN YU[1,3]

[1]State Key Laboratory of Optoelectronic Materials and Technologies and School of Electronics and Information Technology, Sun Yat-sen University, Guangzhou 510275, China.
[2]School of Engineering, University of Glasgow, Rankine Building, Oakfield Avenue, Glasgow G12 8LT, UK.
[3]Department of Electrical and Electronic Engineering, University of Bristol, University Walk, Bristol, BS8 1TR.
*Corresponding author: caixlun5@mail.sysu.edu.cn

Received XX Month XXXX; revised XX Month, XXXX; accepted XX Month XXXX; posted XX Month XXXX (Doc. ID XXXXX); published XX Month XXXX

Integrated devices that emit light beams with orbital angular momentum (OAM) are becoming key components for wide-ranging applications. Here, we propose and demonstrate a highly directional silicon photonic vortex beam emitter based on a 3-turn Archimedean spiral adiabatic waveguide integrated with an angular grating. Such compact emitter is capable of generating vortex beams with small divergence angles and high directivity. Various order OAM modes can be selectively generated by the emitter at different wavelength with side-mode suppression ratio as large as 13.6 dB.

OCIS codes: *(050.4865) Optical vortices; (130.3120) Integrated optics devices; (230.1950) Diffraction gratings;*

http://dx.doi.org/10.1364/OL.99.099999

Over the past two decades, there has been a growing interest in orbital angular momentum (OAM) of light, which is carried by vortex beams possessing helical phase fronts described by an azimuthally dependent phase factor $\exp(i\ell\varphi)$, where ℓ is the topological charge [1]. The transfer of OAM from vortex beams induces rotations in optically trapped dielectric particles, thus it is an effective tool in many applications related to optical manipulation [2,3]. OAM is also being used as a multiplexing approach to increase the capacity of data transmission in both free-space and optical fiber communication systems [4,5]. Recently, several photonic integrated OAM devices have been demonstrated, including a photonic circuit with concentric ring-grooves [6], a micro-ring resonator with angular grating [7], a photonic phased array [8], a GaAs-based ring-shaped Bragg reflector waveguide [9], and a micro OAM laser [10]. For the micro-ring emitter demonstrated in our previous work [7], the principle of operation is to couple the confined whispering gallery mode of the micro-ring resonator to a free-space propagated OAM mode using a second order Bragg grating. In the far-field, the intensity profile of the emitted beam is a series of concentric annuli [see Fig. 2(a)], which is the interference pattern generated by the scattered field of each grating element [11]. This profile makes it difficult to fully collect and utilize the emitted energy, e. g., the coupling of the beam into an OAM fiber is not very efficient [12,13]. To overcome this limitation, we propose and demonstrate an improved emitter based on a multi-turn Archimedean spiral waveguide that emits high directivity and low divergence vortex beams.

The Archimedean spiral is a widely used structure in the design of high-directional microwave antennae [14], which has also been applied in photonics, such as in optical antennae [15], OAM generation [16] and sub-wavelength grating lenses [17]. In the design presented in this letter, the Archimedean spiral replaces the closed cavity of the micro-ring, enabling the spatial modulation of the source in the radial direction, in order to concentrate the emitted power into a ring of stronger intensity with far less pronounced side lobes. This principle is similar to the approach used for generating the so-called perfect vortex beam [18], which is usually realized by adding a radial modulation function to the conventional phase mask implemented with spatial light modulator [19,20].

As shown in Fig. 1, the highly directional vortex beam emitter consists of an input waveguide (I), a 3-turn Archimedean spiral adiabatic waveguide with angular gratings for radiating vortex beams (II) and an extended Archimedean spiral adiabatic inversed taper for the dissipation of remaining light (III). The width of the spiral waveguide is tapered along the azimuthal direction to increase the effective refractive index of the fundamental TE mode so that the angular velocity of the light is constant. Grating elements are embedded in the inner sidewall of the waveguide with equal angular intervals. In polar coordinates (r, φ), a normal Archimedean spiral can be described as

$$\boldsymbol{r = r_0 - \frac{\Lambda}{2\pi}\varphi,} \qquad (1)$$

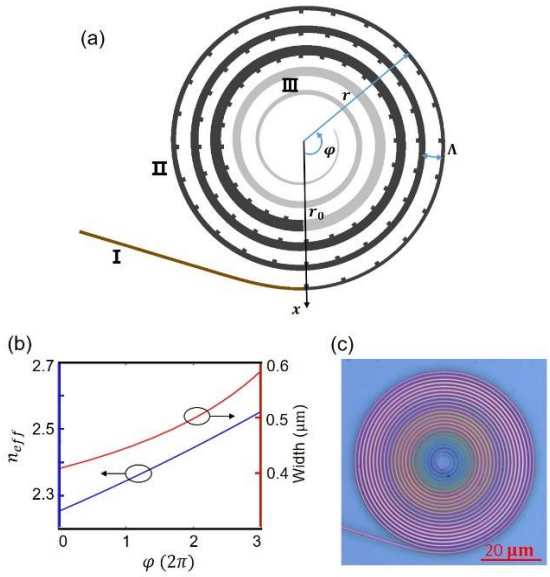

Fig. 1. (a) Structure of the proposed 3-turning Archimedean spiral vortex beam emitter consisting of (I) an input waveguide, (II) 3-turning Archimedean spiral adiabatic waveguide with angular grating embeded in the inner sidewall and (III) an extended Archimedean spiral adiabatic inverse taper. Part of the input light from (I) will be radiated to free-space propagating optical vortex by (II), and the rest of un-radiated light in waveguide will be guided to substrate layer by (III). (b) Simulated and calculated effective refraction index of the fundamental TE mode at a wavelength of 1550 nm (blue curve) and the waveguide width of the 3-turning Archimedean spiral versus angle (red curve). (c) Optical micrographs of the fabricated device.

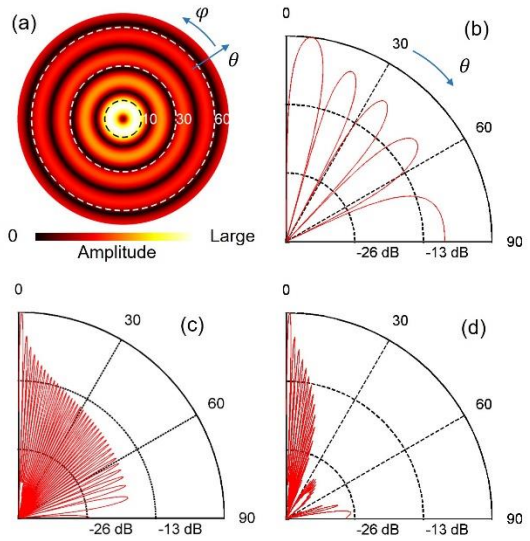

Fig. 2. Simulated radiation pattern when $\ell = 0$. (a) Top view of the far-field distribution from a single ring emitters with R=3.9 μm, and (b) the corresponding radiation pattern. (c) Radiation pattern for a single ring with R=30 μm, and (d) for the 3-turn Archimedean spiral emitter. Due to the circular symmetry, the radiation pattern from 0 to 90 deg is sufficient to illustrate the radiation behavior of the different devices.

where the parameter r_0 controls the starting position of the spiral and Λ is the distance between successive turns. The spiral emitter was designed to operate at a wavelength λ_0=1550 nm, and r_0 was set to 30 μm leaving ample space for the multi-turn spiral. Λ was set to 1.2 μm to ensure low coupling between adjacent spiral waveguide turns. For a 3-turn spiral device, φ ranges from 0 to 6π.. To generate uniform vortex beam, the phase of the fundamental TE mode should change linearly in the azimuthal direction as below

$$\frac{d(\beta S)}{d\varphi} = p, \tag{2}$$

where $\beta = \frac{2\pi}{\lambda_0} n_{eff}$ is the propagation constant of light in the spiral waveguide, n_{eff} is the effective refractive index of the mode, S is the length of the spiral curve and p is the azimuthal phase change constant (phase shift per unit azimuthal angle). According to Eq. (2), the light in the waveguide has to be slowed down to keep a constant rate of phase change as the path shortens along the azimuthal direction in the inner turns. Therefore, the effective index , n_{eff} should increase linearly with φ, which can be realized by varying the size of the waveguide. We use the finite difference eigenmode (FDE) method to calculate the n_{eff} as a function of the waveguide width and bending radius, and then the correct width variation was calculated based on the path [Eq. (1)] and the phase changing condition [Eq. (2)]. As shown in Fig. 1(b), a linear increase of the effective index from 2.25 to 2.55 (blue curve) corresponds to a waveguide width increase from 408 nm to 586 nm (red curve) as a function of the angle. To form second-order grating, the angular interval of the gratings is set to 1.3 degree, so that the number of grating elements per turn, q, is 276. As the phase of the confined TE_0 mode varies linearly with the angle, the azimuthal phase change constant of the beam scattered by the angular grating is

$$v_\varphi = p - q, \tag{3}$$

where q is the number of grating elements in one turn [16]. Eq. (3) indicates that the emission is a helical phase beam with an azimuthal component of the wave vector with topological charge $\ell = p - q$. For a fabricated device, the value of ℓ can be adjusted by injecting light at different wavelengths. Due to the lack of resonance (as opposed to the case of micro-rings), there is no round-trip phase constraint, thus the wave number, p , and the corresponding topological charge of the emitted vortex beam, ℓ, could be a non-integer value. It means that this device is capable of generating fractional OAM beams, which can be decomposed into the superposition of integer OAM modes [21]. These fractional OAM states have found applications in quantum information processing [22] as well as edge-sensitive microscopy [23].

The compact micro-ring emitter in Ref. [7] produces cylindrical vector Bessel (CVB) modes in the far-field, with all the components having amplitudes proportional to the ℓth-order Bessel function of the first kind or to its first derivative [11]. The diffraction angle of all orders can be deduced as $\theta_i^\ell = \tan^{-1}(\chi_\ell^i \times \frac{\lambda}{2\pi R})$, where χ_ℓ^i is the ith extreme point of the ℓth-order Bessel function and R the radius of the micro-ring. For each order vortex beam, the diffraction angle is mainly dependent on the micro-ring radius and can be reduced by an increase of the radius. Fig. 2 shows the radiation patterns from different size emitters when $\ell = 0$, which are calculated by a dipole model described in Ref. [11]. To quantify the collimation in the

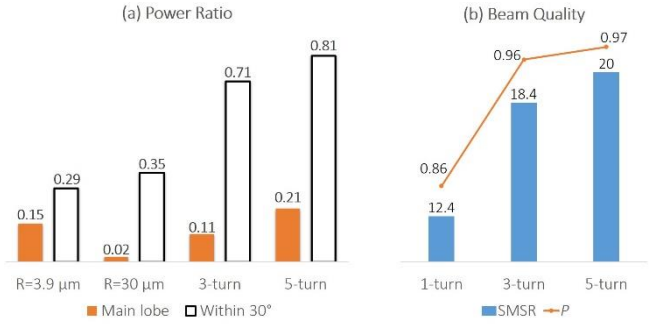

Fig. 3. (a) Simulated power distribution in the main lobe (filled bar) and within ± 30 degree diffraction cone (un-filled bar) from single ring emitters with $R = 3.9$ μm and $R = 30$ μm, and 3-turn and 5-turn spiral emitters with starting radius of 30 μm. (b) Calculated side-mode suppression ratio SMSR (blue bar in dB) and OAM purity P (orange polyline) over the ± 30-degree diffraction cone from 1-turn, 3-turn and 5-turn spiral emitters with the same starting radius of 30 μm

direction to the main lobe, we defined the radiation directivity as

$$\boldsymbol{D = 10\log_{10}\left(\frac{P_{ml}/(2\pi \sin\theta_{ml})}{P_{tot}/2\pi}\right),} \qquad \textbf{(4)}$$

where P_{ml} is the power in main lobe, θ_{ml} is the angle of the diffraction cone of main lobe and P_{tot} is the total radiated power. Comparing Fig. 2(b) with (c), clearly shows that the beam from larger size devices has small diffraction angles. Indeed, θ_{ml} for the single-ring device with $R = 3.9$ μm [16] is about 15 degrees, while for the device with $R = 30$ μm, that equals the starting radius of the Archimedean spiral emitter, the angle reduces significantly to 1.8 degrees. However, the number of side lobes increases with the radius, resulting in a decrease of power in the main lobe [see Fig. 3(a)]. The calculated directivity for the device with $R = 3.9$ μm is -2.3 dB and for device with $R = 30$ μm is -1.9 dB i. e. increasing the device size is unable to effectively improve the directivity. The 3-turn spiral emitter benefits from the fact that the diffraction angle varies with radius, i.e. the far-fields of the 1st, 2nd and 3rd turn waveguide have slightly different diffraction angles, which, after interfering with each other, produce a new distribution with energy concentrated in a smaller diffraction cone [21]. Fig. 2(d) shows a radiation pattern from the 3-turn spiral emitter, with some of the side lobes being significantly suppressed, leading to an improvement in directivity to be 5.3 dB. By adding more turns in the spiral, the directivity can be further increased, e. g. 5-turn spiral emitters have a more conspicuous main lobe compared with 3-turn devices [see Fig. 3(a)] with a directivity of 7.9 dB, as the increase in radial width of the source reduces the high spatial-frequency components.

The quality of the vortex beam from spiral emitters could be degraded due to the circular symmetry breaking. Fig. 3(b) shows the calculated side-mode suppression ratio SMSR (the ratio of the selected OAM mode to the side-mode with highest power) and OAM purity P (the power in desired OAM mode to the total radiated power [24]) over a ± 30-degree diffraction cone. It can be seen that the purity increases with the number of turns, since the effect of the distorted phase distribution on the beam quality is weakened as the intensity is more concentrated in a small region. In particular, for the main lobes of the beams from those spiral devices, the OAM purity is as high as 99.96 % (SMSR > 36 dB).

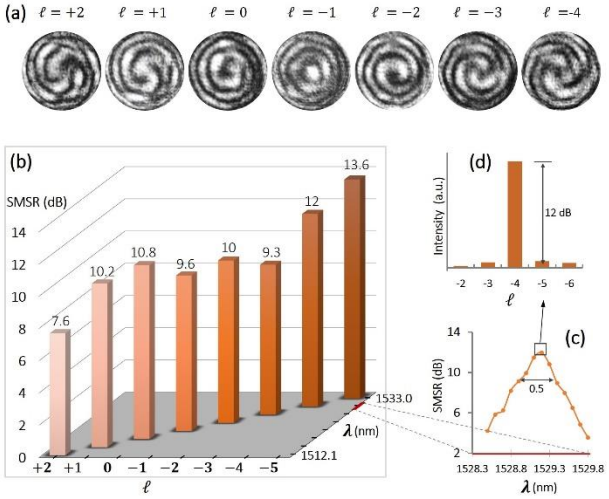

Fig. 4. (a) The interference patterns of the right-hand circularly polarized components with $\ell + 1$ spiral arms. These results were achieved by filtering the emitted vortex through a polarization filter (a quarter-wave plate with a linear polarizer) and beating with a linear polarized Gaussian reference beam. (b) Maximum SMSRs as a function of discrete wavelengths. (c) SMSRs-4 as a function of wavelength. (d) Intensity distribution as a function of OAM index at 1529.2 nm, and the SMSR-4 was calculated.

3-turn Archimedean spiral emitters were fabricated on a 220-nm thick silicon-on-insulator (SOI) material, which was patterned by electron beam lithography and reactive ion etching. Following the procedure described in Ref. [7], we measured the topological charge at different wavelengths by beating the emitted beam with a Gaussian reference beam. The vector beam emitted from the devices can be described as the superposition of two orthogonal scalar OAM modes, which are a left-hand circularly polarized (LHCP) beam with topological charge of $\ell - 1$ and a right-hand circularly polarized (RHCP) beam with topological charge of $\ell + 1$, respectively. Therefore, when the RHCP (LHCP) component of the emitted vortex is made to interfere with a Gaussian beam, it produces spiral intensity patterns with $\ell + 1$ ($\ell - 1$) arms. Fig. 4(a) shows the interference patterns of the RHCP components, which agree with the above discussion, and confirms that this device is capable of generating vortex beams.

We further used the method described in Ref. [25] to examine the purity of the generated OAM modes by measuring the side-mode suppression ratio (SMSR_{ℓ}, subscript indicate the selected OAM index) defined as the ratio of the selected OAM mode to the side-mode with highest power. Fig. 4(b) presents the OAM spectrum of the vortex beam at a wavelength of λ =1529.2 nm with SMSR_{-4} =12 dB, which was measured by recording the on-axis intensity of a series of spatial light modulator diffracted patterns while changing the index of the loaded holographic folk gratings. In the same way, SMSRs_{-4} was measured as the wavelength was fined-tuned, as shown in Fig. 4(c). Its value reaches a maximum at λ_{-4}=1529.2 nm indicating a good quality vortex, and the 3-dB bandwidth is 0.5 nm. At both shorter and longer wavelengths, e. g. 1529.8 nm, SMSRs_{-4} is much reduced as the side-mode component (ℓ_{-3} or ℓ_{-5}) is increased, signifying the formation of fraction OAM modes. Fig. 4(d) shows other maximum SMSRs as a discrete function of wavelength, with values ranging from 7.6 to 13.6 dB. As the waveguide was

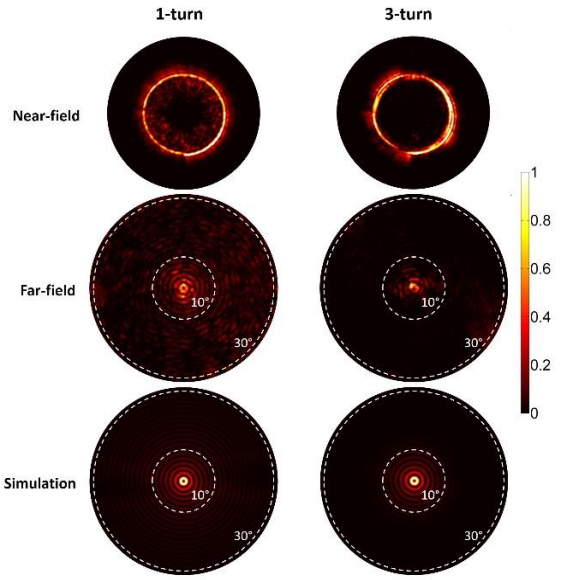

Fig. 5. Intensity distributions of the beam from the 1-turn spiral emitter (first column) and the 3-turn spiral emitter (second column) when $\ell = 0$. The first row shows the near-fields and the second row shows far-fields, which were measured using a near-infrared CCD. The third row are the corresponding simulated far-field. White dotted lines are the diffraction angle at 10-degree and 30-degree, respectively.

designed for a fixed wavelength of 1550 nm, dispersion can leads to a nonlinear variation in phase at other wavelengths, so that the purity of wavelength-dependent OAM was decreased, and it is more serious at shorter wavelengths (or positive ℓ values).

The intensity distribution of the vortex beam generated by the Archimedean spiral emitters is shown in Fig. 5. The patterns were captured by a near-infrared CCD camera at the wavelength where maximum $SMSR_0$ was measured. For comparison, 1-turn spiral emitter, with the same starting radius as of the 3-turn emitter, was fabricated and measured. From the first row in Fig. 5, it can be seen that the near-field of a 3-turn device has a slightly larger radial width than the one of 1-turn device. After propagating to far-field, as shown in the second row in Fig. 5, the radiation intensity of the 3-turn device is mostly concentrated within a 10-degree diffraction cone. However, for the 1-turn device, there is clearly a large intensity distribution outside the 10-degree cone, which is consistent with the simulation results (see the third row in Fig. 5). These results confirm that the directivity of the radiation from the OAM device can be improved by adding a multi-turn waveguide. The emission efficiency [7] of the 3-turn spiral emitter is ~3 %, since the weak grating radiated less light power and most of input light was guided to substrate through (III). The effciency can be improved by introducing strong grating, more turns of spiral waveuigudes and a metellic layer under the grating [26].

In conclusion, we proposed and demonstrated a vortex beam emitter based on a 3-turn Archimedean spiral waveguide with integrated angular gratings. By carefully designing the waveguide width, the emitter is capable of generating vortex beams with high OAM purity, and the OAM value can be adjusted by simply tuning the wavelength of injected light. The radiation from the spiral emitter has a small divergence angle and higher directivity compared to a single ring emitter, which provides an option for efficient OAM transmitters and receivers.

Funding. National Basic Research Program of China (973 Program) (2014CB340000); National Natural Science Foundation of China (NSFC) (11690031, 61490715, 61622510, 61575224, 11690030); EU-H2020 ROAM; EPSRC Cornerstone projects.

Acknowledgment. The authors acknowledge the support from the technical staff of the James Watt Nanofabrication at Glasgow University.

References

1. L. Allen, M. W. Beijersbergen, R. J. C. Spreeuw, and J. P. Woerdman, Phys. Rev. A **45**, 8185–8189 (1992).
2. N. Simpson, K. Dholakia, L. Allen, and M. Padgett, Opt. Lett. **22**, 52–54 (1997).
3. D. G. Grier, Nature **424**, 810–816 (2003).
4. J.Wang, J. Yang, I. M. Fazal, N. Ahmed, Y. Yan, H. Huang, Y. Ren, Y. Yue, S. Dolinar, M. Tur, and A. E.Willner, Nature Photon. **6**, 488–496 (2012).
5. N. Bozinovic, Y. Yue, Y. Ren, M. Tur, P. Kristensen, H. Huang, A. E. Willner, and S. Ramachandran, Science **340**, 1545–1548 (2013).
6. T. Su, R. P. Scott, S. S. Djordjevic, N. K. Fontaine, D. J. Geisler, X. Cai, and S. J. B. Yoo, Opt. Express **20**, 9396–9402 (2012).
7. X. L. Cai, J. W. Wang, M. J. Strain, B. Johnson-Morris, J. B. Zhu, M. Sorel, J. L. O'Brien, M. G. Thompson, and S. Y. Yu, Science **338**, 363–366 (2012).
8. J. Sun, M. Moresco, G. Leake, D. Coolbaugh, and M. R. Watts, Opt. Lett. **39**, 5977–5980 (2014).
9. S. Mochizuki, X. Gu, K. Tanabe, A. Matsutani, M. Ahmed, A. Bakry, and F. Koyama, Appl. Phys. Express **7**, 022502 (2014).
10. P. Miao, Z. F. Zhang, J. B. Sun, W. Walasik, S. Longhi, N. M. Litchinitser, and L. Feng, Science **353**, 464-467 (2016).
11. J. B. zhu, X. L. Cai, Y. J. Chen, and S. Y. Yu, Opt. Lett. **38**, 1343-1345 (2013).
12. C. Brunet, P. Vaity, Y. Messaddeq, S. LaRochelle, and L. A. Rusch, Opt. Express **22**, 26117–26127 (2014).
13. J. Liu, S. M. Li, J. Du, C. Klitis, Cheng Du, Q. Mo, M. Sorel, S. Y. Yu, X. L. Cai, and J. Wang, Opt. Lett. **41**, 1969-1972 (2016).
14. W. L. Stutzman and G. A. Thiele, Antenna Theory and Design, 3rd ed. New York: Wiley, 2012.
15. G. H. Rui, W. B. Chen, D. C. Abeysinghe, R. L. Nelson, and Q. W. Zhan, Opt. Express **20**, 19297-19304 (2012).
16. E. Brasselet, G. Gervinskas, G. Seniutinas, and S. Juodkazis, Phys. Rev. Lett. **111**, 193901 (2013).
17. S. Vo, D. Fattal, W. V. Sorin, Z. Peng, T. Tran, R. G. Beausoleil, and M. Fiorentino, IEEE Photon. Technol. Lett. **26**, 1375–1378 (2014).
18. A. S. Ostrovsky, C. Rickenstorff-Parrao, and V. Arrizón, Opt. Lett. **38**, 534-536 (2013).
19. P. Vaity and L. Rusch, Opt. Lett. **40**, 597-600 (2015).
20. J. Lin, X.-C. Yuan, S. H. Tao, and R. E. Burge, Opt. Lett. **31**, 1600-1602 (2006).
21. J. B. Götte, K. O'Holleran, D. Preece, F. Flossmann, S. Franke-Arnold, S. M. Barnett, and M. J. Padgett, Opt. Express **16**, 993–1006 (2008).
22. B. J. Pors, F. Miatto, G. W. 't Hooft, E. R. Eliel, and J. P. Woerdman, J. Opt. **13**, 064008 (2011).
23. S. F¨urhapter, A. Jesacher, S. Bernet, and M. Ritsch-Marte, Opt. Express **13**, 689–694 (2005).
24. G. Molina-Terriza, J. P. Torres, and L. Torner, Phys. Rev. Lett. **88**, 013601 (2002).
25. M. J. Strain, X. Cai, J. Wang, J. Zhu, D. B. Phillips, L. Chen, M. Lopez-Garcia, J. L. O'Brien, M. G. Thompson, M. Sorel, and S. Yu, Nat. Commun. **5**, 4856 (2014).
26. Y. Ding, H. Ou, and C. Peucheret, Opt. Lett. **38**, 2732 (2013).